

A High-Order Phase Correction Approach for Focusing HS-SAR Small-Aperture Data of High-Speed Moving Platforms

Yi Liang, Zhenyu Li, Letian Zeng, Mengdao Xing, *Member, IEEE*, and Zheng Bao, *Life Senior Member, IEEE*

Abstract—The squinted imaging mode has been successfully applied to synthetic aperture radar (SAR) mounted on moving platforms of high speed. The developed focusing algorithms for squint SAR data usually perform the linear range walk correction (LRWC) in the azimuth time domain as the first step, to mitigate the bulk range-azimuth coupling. Unfortunately, when applied on high-speed platforms with large squint angle and large azimuth scene length, these algorithms for airborne SAR considering only the first-order azimuth dependence of the Doppler frequency-modulation (FM) rate will introduce a large residual phase error, and therefore degrade the final radar image quality. Meanwhile, those algorithms, originally designed for full-aperture data, cannot be applied directly to the small-aperture data. Due to these problems, a high-order phase correction approach (HPCA) combined with SPECAN operation for focusing high-squint SAR (HS-SAR) small-aperture data is developed in this paper to deal with the above issues. In this approach, both the first- and the second-order azimuth dependence of the Doppler FM rate are compensated for, and the same to the cubic phase term, by introducing a correction phase term in the azimuth frequency domain. The presented approach has been successfully used to focus the real airborne radar data recently.

Index Terms—Azimuth dependence, high-squint synthetic aperture radar (SAR), high-order phase correction approach (HPCA), small-aperture data, SPECAN.

I. INTRODUCTION

SYNTHETIC aperture radar (SAR) is an active microwave sensor, capable of working day and night and nearly independent of weather conditions [1]. With the rapid development of SAR technology, the real-time imaging of high-squint SAR (HS-SAR) with large azimuth scene length on high-speed moving platforms, such as satellites and missiles, has received much attention recently, and has become a challenging task which cannot be achieved easily by the conventional algorithms. In order to solve these problems, small-aperture data processing with mosaicking technique is a potential approach. Meanwhile, it can also solve the problem of the nonlinear flight track imaging. If the full azimuth resolution is not required, it would be possible by using only one small-aperture data, which are a part

of the full-aperture data so as to implement quick look imaging. Therefore, it is significant to have a study on the small-aperture imaging algorithms for HS-SAR real-time processing.

A number of algorithms have been proposed for HS-SAR that are mounted on moving platforms of high speed, such as the modified DBS algorithm [2], SPECAN algorithm [3], Omega-K algorithm [4], [5], and CA Omega-K algorithm [6]. These algorithms have improved the performance of HS-SAR imaging. However, all these algorithms have their disadvantages and limitations. For example, the modified DBS algorithm is suitable for the case of low resolution. The SPECAN algorithm is easy to implement and is efficient for small-aperture data processing, but might fail in some complex cases due to its simple signal model. The Omega-K algorithm can process any squint angle in theory. Since it processes the SAR data in two-dimensional (2-D) wavenumber domain, it can hardly accommodate the circumstance with range parameter changing, particularly the squint angle, and additionally the Stolt interpolation reduces the efficiency.

Based on the similarity with airborne SAR imaging, the algorithms for HS-SAR on high-speed moving platforms can make reference to those of airborne-squint SAR. In recent years, the algorithms for airborne-squint SAR have seen a great development. For example, CSA [7], BP [8], NLCS [9], [10], and their modified forms (ECS [11], FFBP [12], ENLCS [13]–[19], MNLCS [20], etc.). They can improve the accuracy of the airborne-squint SAR final focused images, but still have their limitations. The RDA and the CSA have relatively simpler implementation and higher efficiency, but they are only suitable for processing the low-squint SAR data. BP and FFBP are both the time-domain algorithms and their efficiency are lower than the frequency-domain counterparts [12]. For the time-domain algorithms, it is difficult to be compatible with the data-driven motion compensation when accurate trajectory information is missing. Compared with the above algorithms, the NLCS algorithm is a good choice for the airborne HS-SAR data focusing, but not suitable for HS-SAR on high-speed moving platforms due to its limited accuracy of the azimuth dependence. Some publications [13]–[19] have attempted to improve the precision of NLCS operations and extend the azimuth length. Unfortunately, all the above algorithms are based on the full-aperture processing and cannot be used directly in the small-aperture processing. However, for HS-SAR on high-speed moving platforms real-time processing, the small-aperture data processing is more attractive.

Manuscript received August 07, 2014; revised July 02, 2015; accepted July 15, 2015. This work was supported in part by the National Natural Science Foundation of China under Grant 61301293 and in part by the Fundamental Research Funds for the Central Universities under Grant K5051302046. (Corresponding author: Yi Liang.)

The authors are with the National Laboratory of Radar Signal Processing, Xidian University, Xi'an 710071, China (e-mail: yiliang@xidian.edu.cn).

Color versions of one or more of the figures in this paper are available online at <http://ieeexplore.ieee.org>.

Digital Object Identifier 10.1109/JSTARS.2015.2459765

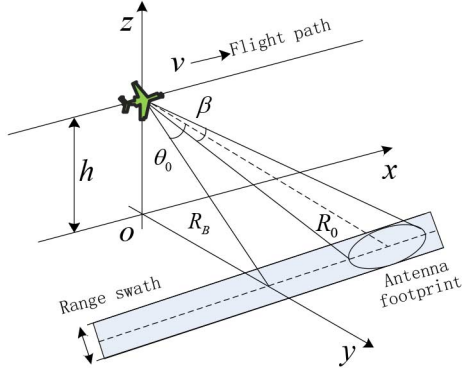


Fig. 1. Geometric model of HS-SAR.

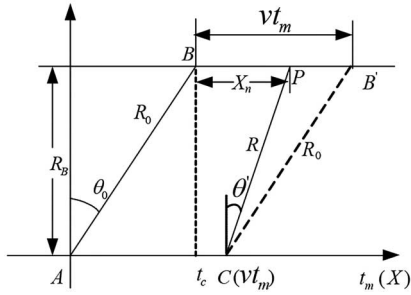


Fig. 2. Data recording plane formed by the flight path and the target.

This paper is mainly focused on the HS-SAR large azimuth length imaging on high-speed moving platforms using only one small-aperture data.

II. APPROXIMATION-FREE SLANT RANGE MODEL AND ECHO SIGNAL MODEL

A. Approximation-Free Slant Range Model

Fig. 1 illustrates the imaging geometry of a typical HS-SAR working in the stripmap mode. The SAR sensor travels along the azimuth direction which is parallel to the x -axis. h is the constant flight altitude, v is the speed, θ_0 is the squint angle of the antenna beam center, β is the azimuth beamwidth, and R_B is the closest distance from the target to the flight path. R_0 is the slant range at the beam center crossing time. It should be pointed out that, due to the short accumulated time (small aperture), we assume that the sensor moves in a straight line with a constant velocity by neglecting the variation of the velocity and direction, and the motion errors are not considered, since we mainly focus on the imaging algorithm investigation here.

For the convenience of analysis, we take a look at the data recording plane formed by the flight path and the target, as shown in Fig. 2. Assume that A is the azimuth starting point, namely azimuth slow time $t_m = 0$. At this point, the antenna beam center line intersects the line which crosses target P and is parallel to the flight trajectory at point B. Set B as the azimuth starting point of this parallel line, which is equivalent to establishing a conical coordinate system. In Fig. 2, θ' is the instantaneous look angle of the target.

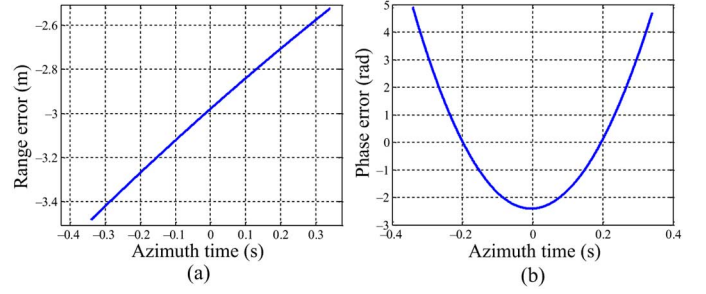


Fig. 3. Simulated results for $x_n = 6000$ m. (a) Residual envelope errors of Taylor series with the second-order approximation. (b) Residual phase errors of Taylor series with the third-order approximation.

After an azimuth time of t_m , the platform moves to point C, and the corresponding x coordinate is vt_m . Suppose the distance between target P and point B is x_n , then the instantaneous slant range can be obtained from the triangle PCB'

$$R(t_m; R_0) = \sqrt{(vt_m - x_n)^2 + R_0^2 - 2R_0(vt_m - x_n) \sin \theta_0}. \quad (1)$$

This instantaneous slant range can be expanded to a constant term, a linear term (the linear range walk), a quadratic term (the range curvature), and the high-order terms with respect to the azimuth slow time. In some low-squint SAR cases, the expansion of (1) for envelope up to the second order and for phase up to the third order are adopted, and all of the residual higher order terms are neglected due to their weak impacts [13]–[19]. However, the impacts of these terms become considerable with large squint angle or higher resolution. In order to analyze the residual envelope errors and phase errors, we consider a Ku-band SAR system with the parameters $R_0 = 30$ km, $\theta_0 = 80^\circ$, $v = 1000$ m/s, $f_c = 17$ GHz, and $x_n = 6000$ m. Fig. 3(a) and (b) shows the diagrams for the residual envelope errors and the residual phase errors.

The envelope relative errors are around 1 m in this case. It is widely accepted that the envelope errors can only be neglected when the migration is less than one-fourth of the range resolution cell, which implies a resolution less than 4 m. On the other hand, the residual phase errors are much larger than $\pi/4$ (the linear component has been dropped, since it only results in azimuth shift and not defocusing), which cannot be neglected at all. Therefore, in the high-squint mode, the above approximation is not sufficient, and a more exact model should be introduced. Based on this consideration, this paper uses the approximation-free slant range model to investigate the small-aperture data imaging algorithm.

B. Echo Signal Model

Suppose that the transmitted pulses are linearly modulated in frequency. The received signal from target P in the range frequency domain is given by

$$Ss(f_r, t_m; R_0) = W_r(f_r) w_a(t_m) \exp\left(-j\pi \frac{f_r^2}{\gamma}\right) \cdot \exp\left(-j\frac{4\pi}{c}(f_c + f_r)R(t_m; R_0)\right) \quad (2)$$

where $W_r(\cdot)$ represents the range envelope in frequency domain, $w_a(t_m)$ denotes the azimuth envelope in time domain, γ is the range chirp rate, c is the speed of light, f_r and f_c are the range frequency and the carrier frequency, respectively. Observing (2), the first exponential term is the range frequency-modulation (FM) term, which can be easily compensated for by multiplying its complex conjugate. The second exponential term comes from the azimuth modulation.

III. RANGE SIGNAL PROCESSING

The range processing of HS-SAR involves two steps: 1) the range cell migration correction (RCMC) and 2) the range focusing, which includes the range compression (RC) and the secondary range compression (SRC). The RCMC contains the linear range walk correction (LRWC) and the range curvature correction (RCC). In general, the LRWC is often performed in the range frequency and azimuth time domain as the first step by using a linear phase multiplication, and the RCC operation is performed in the 2-D frequency domain by multiplying a selected reference range compensating factor.

A. LRWC

It is a challenging task for HS-SAR data focusing due to the strong coupling between the range and azimuth. The LRWC operation can reduce the cross coupling and simplify the following processing operation. According to [13]–[19], the value of the linear range walk is $v \sin \theta_0 t_m$, so the compensating factor is given by

$$H_{LRWC}(f_r, t_m) = \exp \left(-j \frac{4\pi v \sin \theta_0}{c} (f_c + f_r) t_m \right). \quad (3)$$

B. RCC, RC, and SRC

Transforming the echo signal after the LRWC into the 2-D frequency domain yields

$$\begin{aligned} SS(f_r, f_a; R_0) &= W_r(f_r) W_a(f_a) \exp \left(-j\pi \frac{f_r^2}{\gamma} \right) \\ &\cdot \exp \left(-j \frac{4\pi x_n \sin \theta_0}{c} f_r \right) \\ &\cdot \exp(-j4\pi R_0 \cos \theta_0 \Phi_0) \\ &\cdot \exp \left(-j4\pi R_0 \cos \theta_0 \left(\Phi_1 + \frac{\sin^2 \theta_0}{\cos \theta_0 \cdot c} \right) f_r \right) \\ &\cdot \exp(-j4\pi R_0 \cos \theta_0 \Phi_2 f_r^2) \\ &\cdot \exp \left(-j \frac{2\pi}{v} (f_a + f_{dc}) (R_0 \sin \theta_0 + x_n) \right). \end{aligned} \quad (4)$$

The detailed derivation of (4) is shown in Appendix A, including the expressions of Φ_0 , Φ_1 , and Φ_2 . In (4), f_a denotes the azimuth frequency, $W_a(\cdot)$ represents the azimuth envelope in frequency domain, and f_{dc} is the Doppler center frequency, with the value $f_{dc} = 2v \sin \theta_0 / \lambda$ (λ is the carrier

wavelength). Furthermore, the second exponential term denotes the deformation of the range position. The third exponential term shows the azimuth frequency modulated item. The fourth exponential term is the range curvature and the fifth exponential term is called the SRC. The last exponential term reflects the real azimuth position, the azimuth deformation, and the constant phase.

From (4), it is easy to get the RCC, the range compression and the SRC factors, which have the complex conjugate forms of the first, the fourth, and the fifth exponential terms. It should be noted that, the RCC and SRC factors are both range dependent, and we use the compensating factors at the reference range as an acceptable approximation, where the reference range is the slant range at the center line of the scene. Usually, when the range swath is so large that the range dependence cannot be neglected, a convincing method is used to divide the range into several small blocks and each block has its corresponding reference range [18].

After the range multiplication processing and transforming the result into the range time domain by the inverse FFT, we have

$$\begin{aligned} sS(\hat{t}, f_a; R_0) &= \text{Sinc} \left\{ B_r \left(\hat{t} - \frac{2(R_0 + x_n \sin \theta_0)}{c} \right) \right\} \\ &\cdot W_a(f_a) \exp(-j4\pi R_0 \cos \theta_0 \Phi_0) \\ &\cdot \exp \left(-j \frac{2\pi}{v} (f_a + f_{dc}) (R_0 \sin \theta_0 + x_n) \right) \end{aligned} \quad (5)$$

where \hat{t} represents the range fast time. Observing the range envelope $\text{Sinc}(\cdot)$ in (5) (the rectangular form of $W_r(\cdot)$ has been assumed), B_r is the transmitted signal bandwidth, and $R_0 + x_n \sin \theta_0$ is the new slant range, which varies with the azimuth position x_n . It means that the points lying in the same range cell after range processing have different original slant ranges. This dependence can induce the variation of the azimuth FM rate and phase coefficients of high-order terms, and give rise to the azimuth filtering mismatch for different targets in the same range cell.

IV. AZIMUTH COMPRESSION BASED ON HIGH-ORDER PHASE CORRECTION TECHNIQUE

According to Section III, we know that the value of Doppler FM rate and the coefficients of high-order phases vary with the azimuth position after the range processing, resulting in the failure of uniform azimuth processing. In order to solve this problem, a high-order phase correction approach (HPCA) for small-aperture data is presented. Its main idea is to eliminate the azimuth dependence by introducing a correction phase in the azimuth frequency domain, to realize the azimuth focusing via a common reference function. In the following, the selection of the image focused domain and the azimuth dependent characteristic are analyzed in detail first.

A. Selection of Focused Domain

It is convenient for HS-SAR on high-speed moving platforms to adopt the small-aperture data processing. When the matched

filtering method in time domain is selected, the small-aperture data have to be extended at least to the length of a full aperture by padding zeroes. As the squint angle gets larger, the number of padded zeroes will increase rapidly, which will heavily reduce the efficiency of the processing method. The frequency domain focusing SPECAN algorithm deals with such a situation without zero padding, so it has great advantages over the time-domain focusing method. Therefore, for the small-aperture data imaging, we choose the frequency domain as the focused region. It should be noted that, although the presented phase correction method needs zero padding to remove the azimuth dependence, the extension is much smaller than that of the time-domain focusing method. Here, considering the parameters given in Section II and assuming $D_a = 0.2$ m, $R_s = 30$ km, $PRF = 3$ kHz, the extension of the matched filtering method in azimuth time domain is

$$N_{zeros} = \frac{\lambda}{D_a} \cdot R_s \cdot \frac{1}{\cos \theta_0} \cdot \frac{PRF}{v} = 45\,731. \quad (6)$$

In contrast, the extension adopting the proposed focusing method in frequency domain is 6675 (the computation expression is shown in Section IV-D). So, it can conclude that the frequency-domain focusing has much higher efficiency than the time-domain focusing for the small-aperture data processing.

B. Analysis of the Azimuth Dependence

For a further analysis, we introduce the following substitution, i.e., let

$$R'_0 = R_0 + x_n \sin \theta_0. \quad (7)$$

The phase terms of (5) are expanded at $f_a = 0$ and its fourth coefficients are kept. Then, the signal can be written as

$$sS(\hat{t}, f_a; R'_0) = \text{Sinc} \left\{ B_r \left(\hat{t} - \frac{2R'_0}{c} \right) \right\} W(f_a) \cdot \exp \left(-j \sum_{n=0}^4 \phi'_n(R'_0, x_n) f_a^n \right) \quad (8)$$

where $\phi'_n(R'_0, x_n) = \phi'_{n0}(R'_0) + \phi'_{n1}(x_n)$ (the corresponding expressions are shown in Appendix B). Inspecting (8), the coefficients of the phase terms vary with x_n . This phenomenon is called the azimuth dependence. According to (8), the residual azimuth dependent phase errors are as follows:

$$\Delta \phi'_n = |\phi'_n(R'_0, x_n) f_a^n - \phi'_n(R'_0, 0) f_a^n|_{f_a=v \cos \theta_0 / \rho_a}, \quad n = 2, 3, 4. \quad (9)$$

Generally, the azimuth dependent phase errors get larger when the azimuth position increases. In most cases, the azimuth dependent quadratic phase error (QPE) and the cubic phase error (CPE) are larger than $\pi/4$, while the biquadratic phase error (high-order phase error, HPE) is less than $\pi/4$ [17]. So, it is reasonable to ignore azimuth dependent HPE in most HS-SAR cases and the coefficients of azimuth phase can be approximated by

$$\phi'_2 = \phi'_{20} + \phi'_{21}, \quad \phi'_3 = \phi'_{30} + \phi'_{31}, \quad \phi'_4 \approx \phi'_{40}. \quad (10)$$

C. Derivation of the HPCA

In this section, we investigate the HPCA. Based on the analysis of azimuth dependence, the azimuth-independent components of the cubic phase and the high-order phase in (10) can be simply compensated for by multiplying with their conjugates. The compensating factor is given by

$$H_{high}(f_a; R'_0) = \exp(j(\phi'_{30} f_a^3 + \phi'_{40} f_a^4)). \quad (11)$$

Further, transforming the result into the azimuth time domain by the POSP, we have

$$ss(\hat{t}, t_m; R'_0) = \text{Sinc} \left[B_r \left(\hat{t} - \frac{2R'_0}{c} \right) \right] w(t_m) \cdot \exp \left[-j\pi \frac{4R'_0}{\lambda} + j\pi K_a \left(t_m - \frac{x_n}{v} \right)^2 + j\pi K_t \left(t_m - \frac{x_n}{v} \right)^3 \right] \quad (12)$$

where K_a and K_t represent the azimuth FM rate and the coefficient of third-order term, respectively, and their expressions are

$$K_a = -\frac{2v^2 \cos^2 \theta_0}{\lambda(R'_0 - x_n \sin \theta_0)}, \quad K_t = \frac{2v^3 \sin^2 \theta_0 \cos^2 \theta_0}{\lambda(R'_0 - x_n \sin \theta_0)^3} x_n. \quad (13)$$

The approximations below are used

$$\begin{cases} K_a \approx K_{ac} + K_{al} \cdot x_n + K_{as} \cdot x_n^2 \\ K_t \approx K_{tl} \cdot x_n \end{cases} \quad (14)$$

where $K_{ac} = -\frac{2v^2 \cos^2 \theta_0}{\lambda R'_0}$, $K_{al} = -\frac{2v^2 \cos^2 \theta_0 \sin \theta_0}{\lambda R'^2_0}$, $K_{as} = -\frac{2v^2 \cos^2 \theta_0 \sin^2 \theta_0}{\lambda R'^3_0}$, and $K_{tl} = \frac{2v^3 \sin^2 \theta_0 \cos^2 \theta_0}{\lambda R'^3_0}$. Equation (14) expands the azimuth FM rate in terms of x_n up to the second order, and the coefficient of the cubic phase up to the first order. Compared with the traditional algorithm [13], [14], [16], [17], which only considers the first-order term of the azimuth FM rate and ignores the azimuth dependence of the coefficient of high-order phases, the approximation of (14) has higher accuracy in the case of HS-SAR with large azimuth length.

1) *Illustration of the Azimuth Dependence Correction Based on the HPCA:* From (12), the azimuth signal frequency is

$$f = K_a \left(t_m - \frac{x_n}{v} \right) + \frac{3K_t}{2} \left(t_m - \frac{x_n}{v} \right)^2. \quad (15)$$

In (15), K_a is the first-order coefficient of t_m , giving the linearity of the time-frequency distribution curve (TFDC) and K_t has the curved characteristic. In order to explain the idea, we assume that there are three targets located at the reference range with one in the azimuth center and the other two on both sides. Their corresponding TFDC are denoted as $TF|_{x_0}$, $TF|_{-x_n}$, and $TF|_{x_n}$, respectively, as shown in Fig. 4(a). The TFDC have different gradients and curvatures due to the different azimuth positions. For the center target $x_n = 0$, its TFDC only has the linear characteristic and its gradient is denoted as k_{x0} . Since the small-aperture data are considered, the projections of these targets' TFDC on the time axis will be overlapped, and separate from each other on the frequency axis. After applying FFT, the

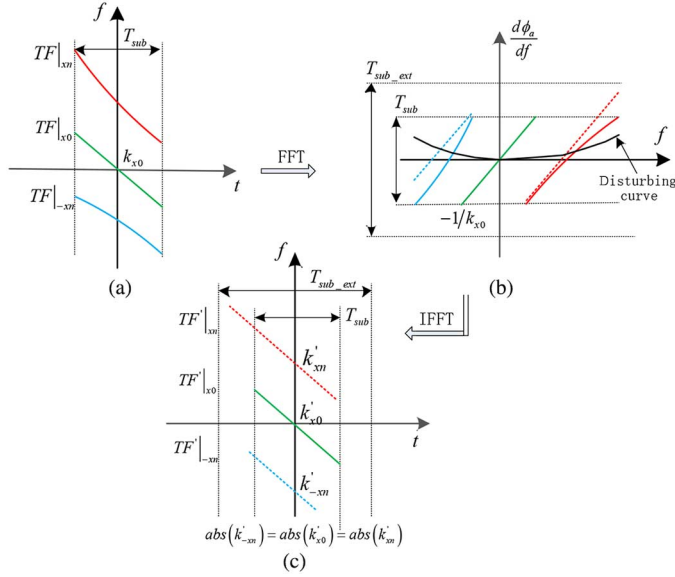


Fig. 4. Diagrams for the procedures of azimuth dependence into independence. (a) TFDC of the three targets. (b) DPFDC of the three targets. (c) New TFDC of the three targets.

time–frequency axes will be overturned, and the corresponding projections of the differential of phase versus frequency distribution curves (DPFDC) along the horizontal axis are separate from each other. The innovative method is to introduce another DPFDC, whose main function is to adjust the current DPFDC to have the same shape. As shown in Fig. 4(b). The black solid line describes the introduced correction curve. This correction curve adjusts the DPFDC of the three targets to have the same gradient ($-1/k_{x0}$), but with a displacement along the vertical axis, as the dashed lines shows. This displacement will have two impacts on the results: on the one hand, it leads to a deformation on the focused image (described in Section IV-E); on the other hand, it can also make the DPFDC exceed the boundary, namely, the small-aperture time T_{sub} , and alias from the other side, if the boundary is not extended in advance. The aliased DPFDC will cause “ghost” images, and we need to extend the vertical boundary beforehand to eliminate the “ghost.” This can be easily implemented by zero padding on the original time-domain data. In Fig. 4(b), T_{sub_ext} represents the time after azimuth zero padding and the detailed analysis of the number of padded zeroes is carried out in Section IV-D.

For the adjusted DPFDC, an inverse FFT is performed to transform the data into the time domain, and the new TFDC, $TF'|_{x_0}$, $TF'|_{-x_n}$, and $TF'|_{x_n}$, will have the same gradient (the linear distribution), i.e., $abs(k'_{-x_n}) = abs(k'_{x_0}) = abs(k'_{x_n})$. Additionally, the projection of the new TFDC on the time axis exceeds the small-aperture time (i.e., T_{sub}), as shown in Fig. 4(c). At this time, the uniform azimuth focusing can be done because all of the targets' TFDC have the same gradient.

2) *Azimuth Focusing*: An azimuth filtering processing up to the fourth order should be first applied in the frequency domain, which is the introduced correction phase. The azimuth filtering factor is given by

$$H_{fil}(f_a; R'_0) = \exp(j\pi p f_a^3 + j\pi q f_a^4) \quad (16)$$

where p and q represent the undetermined coefficients, respectively. The first exponential term in (16) is used to correct the first-order azimuth dependence of the FM rate. The second-order azimuth dependence of the FM rate, as well as the first-order azimuth dependence of the cubic phase coefficient is corrected by the second exponential term. Multiplying the signal undergoing (11) compensation by (16) and transforming the result into the azimuth time domain by the POSP yields

$$ss(\hat{t}, t_m; R'_0) = \text{Sinc} \left[B_r \left(\hat{t} - \frac{2R'_0}{c} \right) \right] w(t_m) \cdot \exp[-j\Phi(t_m; R'_0, x_n)] \quad (17)$$

where

$$\begin{aligned} \Phi(t_m; R'_0, x_n) \approx & A(t_m, t_m^2, t_m^3, t_m^4, R'_0, p, q) + B(R'_0, p, q) x_n t_m \\ & + C(R'_0, p, q) x_n^2 t_m \\ & + D(R'_0, p, q) x_n t_m^2 + E(R'_0, p, q) x_n^2 t_m^2 \\ & + F(R'_0, p, q, x_n, x_n^2, x_n^3, x_n^4). \end{aligned} \quad (18)$$

We analyze the phase terms in (18): the first term is due to the azimuth-independent phase modulation, which can be compensated for uniformly; the second term is the linear coupling of azimuth position x_n with azimuth time t_m , and describes the target real azimuth position; the third term is the main factor that causes the geometric distortion of nonuniform shift. Because of the form of $x_n^2 t_m$, the shift is always nonsymmetric, and the targets furthest away from the center suffer from the most shift; the fourth and fifth terms, reflecting the first- and second-order azimuth dependence of the Doppler FM rate as well as that of the third-order phase coefficient in the time domain, are the main factors that defocus the azimuth image. The sixth term can be dropped in focusing thanks to its independence on azimuth slow time.

To eliminate the azimuth dependence, we set the coefficients $D(R'_0, p, q)$ and $E(R'_0, p, q)$ to be zero. Then, we have the following equations:

$$\begin{cases} D(R'_0, p, q) = 0 \\ E(R'_0, p, q) = 0. \end{cases} \quad (19)$$

Solving (19) for p and q

$$\begin{cases} p = \frac{K_{al}v}{3K_{ac}^3} \\ q = \frac{3K_{tl}K_{ac}v + 3K_{al}^2v^2 - K_{as}K_{ac}v^2}{6K_{ac}^5}. \end{cases} \quad (20)$$

Further, we substitute p and q into A , and obtain the azimuth deramp factor

$$H_{deramp}(t_m; R'_0) = \exp \left(-j\pi K_{ac} t_m^2 - j\pi \frac{K_{al}v}{3} t_m^3 + j\pi \frac{3K_{tl}K_{ac}v + 3K_{al}^2v^2 - K_{as}K_{ac}v^2}{6K_{ac}} t_m^4 \right). \quad (21)$$

Finally, multiplying (17) by the azimuth deramp factor and transforming the resulting signal into the frequency domain, we can get the 2-D well focused SAR image

$$sS(\hat{t}, f_a; R'_0) = \text{Sinc} \left[B_r \left(\hat{t} - \frac{2R'_0}{c} \right) \right] \cdot \text{Sinc} \left[\frac{1}{B_a} \left(f_a - K_{ac} \cdot \frac{x_n}{v} - K_{al} \cdot \frac{x_n^2}{v} \right) \right] \quad (22)$$

where B_a is the azimuth small-aperture Doppler bandwidth for a single target. It is evident that the final focused image is the function of 2-D *Sinc* (similarly, the rectangular form of $W_a(\cdot)$ is assumed). However, it should be noted that the final focused image has known geometric distortions both in the range and azimuth directions.

D. Azimuth Zero Padding Operation

From the analysis in Section IV-C, we know that the zero padding operation is used to avoid the “ghost” phenomenon in azimuth direction. Here, the number of padded zeroes is analyzed in detail.

From (16), the introduced correction phase is given by

$$\psi_{azi}(f_a) = \pi p f_a^3 + \pi q f_a^4. \quad (23)$$

The differential of phase versus frequency is

$$\frac{1}{2\pi} \frac{d\psi_{azi}(f_a)}{df_a} = \frac{3}{2} p f_a^2 + 2q f_a^3. \quad (24)$$

For the small-aperture data after the Doppler center compensation, the value of f_a is within the range of $[-B_{azi_sub}/2, B_{azi_sub}/2]$ (B_{azi_sub} is the small-aperture data Doppler bandwidth). Then, the unilateral maximum extended time can be expressed as

$$T_{ext} = \max \left(\left| \text{abs} \left(\frac{3}{2} p f_a^2 + 2q f_a^3 \right) \right|_{f_a = -B_{azi_sub}/2}, \left| \text{abs} \left(\frac{3}{2} p f_a^2 + 2q f_a^3 \right) \right|_{f_a = B_{azi_sub}/2} \right). \quad (25)$$

So, the total number of padded zeros is given by

$$N_{pad} = 2 \cdot T_{ext} \cdot PRF. \quad (26)$$

In general, compared with the full-aperture processing, the number of padded zeroes N_{pad} is much smaller than N_{zeros} , so it can conclude that the frequency-domain focusing has much higher efficiency than the time-domain focusing when applied to the small-aperture data.

E. Azimuth Image Deformation

After transforming the azimuth dependent phase in the frequency domain back into the time domain, the corresponding phase not only includes the coupled term $t_m x_n$ but also contains $t_m x_n^2$, where the expected term $t_m x_n$ reflects the real

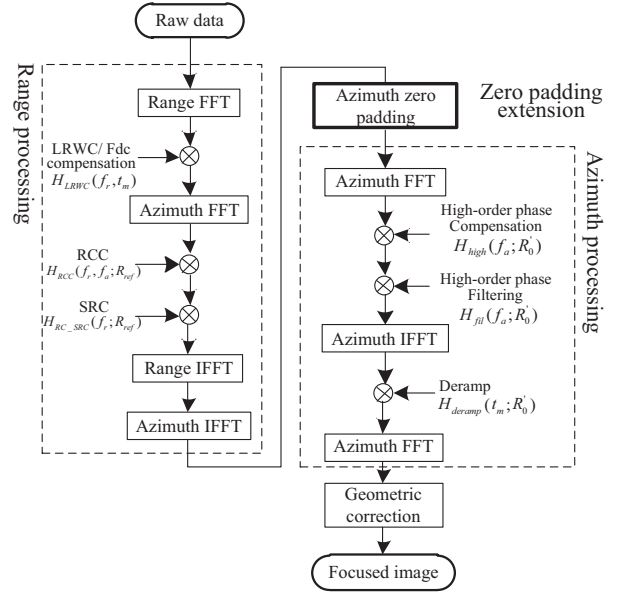


Fig. 5. Flowchart of the HS-SAR small-aperture data imaging approach based on HPCA.

azimuth position but $t_m x_n^2$ is unnecessary and causes deformation in azimuth direction. This deformation varies with the azimuth position and the targets furthest away from the azimuth scene center suffer from the most shift. The shift is given by

$$\Delta x = \frac{K_{al}}{K_{ac}} \cdot x_n^2. \quad (27)$$

Two methods can be adopted to correct this shift. One is the nonuniform interpolation in the image domain, but this method will reduce the processing efficiency rapidly. The other is the combination of the deformation correction with the image geometric correction processing, which is more efficient than the first one.

Totally, the flowchart of the proposed HPCA is shown in Fig. 5.

V. SIMULATION AND RAW DATA PROCESSING

The presented approach is verified by using the simulated data with the parameters given in Table I. Further, it is confirmed by real data from an airborne HS-SAR experiment.

A. Simulation Experiment

The simulation uses a set of five targets along the flight direction, marked as $p_n (n = 1 - 5)$ in Fig. 6. Targets 1–5 have the same interval distance of 3000 m, and the azimuth scene extension is 12 km.

In order to reflect the focusing quality in detail, here, we take target 1, 3, and 5 for a performance examination, without using any windowing manipulation. The target 3 at the scene center is selected as the reference target. Fig. 7 shows the profiles of the azimuth impulse response of the three targets using the reference methods [13], [14], [16], and [17]. Ignoring the

TABLE I
SAR SIMULATION PARAMETERS

Wavelength (λ)	0.0175 m
Range bandwidth (B_r)	80 MHz
Sampling frequency (F_s)	100 MHz
Pulse width (T_p)	25 μ s
Antenna azimuth length (D_a)	0.2 m
Pulse repeat frequency	3 kHz
Height	5 km
Beam center slant range of the center line (R_s)	30 km
Squint angle (θ)	80°
Platform velocity (v)	1000 m/s

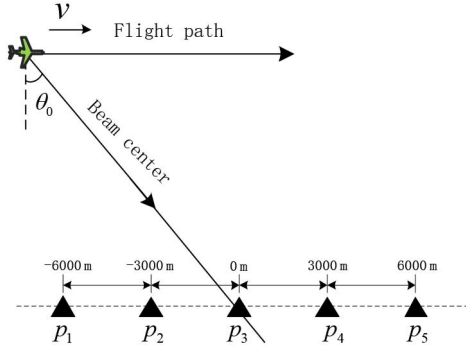


Fig. 6. Flight geometry and target distribution.

second-order azimuth dependence of the FM rate and azimuth dependence of the coefficient of the cubic phase, for the border targets, i.e., targets 1 and 5, there exists a great approximation error. It can be found from Fig. 7 that the profiles of the azimuth impulse response of targets 1 and 5, compared with that of target 3, show two limitations: 1) the first null points have been raised, which degrades the integrated sidelobe ratio (ISLR); 2) the first sidelobes are also raised, which affect the peak side-lobe ratio (PSLR) and further reduces the azimuth resolution. For target 1, the deteriorated PSLR reaches -6.7 dB. This cannot be accepted in practice. Moreover, as the distance from the reference position increases, the target focusing quality degrades quickly due to the influence of the mismatched reference function.

In contrast, the imaging results obtained by our proposed approach are shown in Figs. 8 and 9. Compared with Fig. 7, the first sidelobes and the first null points of targets 1 and 5 in Fig. 8 are heavily suppressed and their azimuth impulse responses are very close to that of target 3. Fig. 9 gives the contour plots of target 1, 3, and 5 using the proposed method. The mainlobes and sidelobes are well separated from each other, and they present an ideal “cross,” which indicates that all the three targets are well focused.

To further evaluate the performance of the proposed algorithm, the measured parameters of PSLR, ISLR, and the spatial resolution (3 dB width) of these targets are calculated, and the results are listed in Table II. It is found that nearly theoretical values of PSLR (-13.26 dB), ISLR (-9.8 dB), and spatial resolutions (1.875 m) are obtained, which demonstrates the validity of the proposed method. In contrast, the performance parameters of the reference methods [13], [14], [16], and [17] are also shown. We can find that the performance parameters of the proposed approach are obviously superior to that of the reference one.

B. Raw Data Processing

The radar works in the Ku-band, the signal bandwidth is 110 MHz, and the spatial squint angle projected on the ground is 70°. The center slant range is about 12 km, and the whole scene is about 3 km in range and 1 km in cross range (one along the line of sight of the radar and another along its perpendicular direction). The resolution is about $1.5 \text{ m} \times 1.5 \text{ m}$. Fig. 10(c) shows the whole ground range image obtained from one small-aperture data processed by the presented approach. The whole image focuses well and the highway can be distinguished clearly.

In contrast, Fig. 10(a) shows the result of the raw data processed without compensation for the azimuth dependence and Fig. 10(b) gives the result processed by the reference algorithms [13], [14], [16], and [17]. In Fig. 10(d), we select the azimuth border of the scene from Fig. 10(a), (b), and (c) by the red-dashed oval for the detailed comparisons and denote the selected scenes as 1, 2, and 3, which corresponds to Fig. 10(a), (b), and (c), respectively. It is obvious that image 1 is seriously defocused as there is no compensation for the azimuth dependence. When considering the first-order azimuth dependence of the FM rate, the image 2 quality is improved, as shown in the middle of Fig. 10(d), but it is still defocused. From the image 3 processed by the HPCA, the azimuth border of the scene is focused better and the image 3 obtains the best result.

Finally, we select a scene by the red-dashed rectangle from (c) and denote it as 4 and perform the image geometric correction processing. In Fig. 10(e), image 4 is superpositioned on an optical image from the Google Earth Map. The geographical features can be clearly distinguished and the SAR image matches the Google Earth Map very well.

VI. DISCUSSION AND CONCLUSION

In this paper, the HPCA for HS-SAR small-aperture data processing on the high-speed moving platforms has been discussed. First of all, we presented a deep analysis on the slant range model without approximation. Based on the 2-D frequency-domain expression of the echo signal, the LRWC and RCC factors are obtained. For the azimuth processing, a HPCA method is proposed. Its main idea is to introduce a correction phase in the frequency domain to eliminate the azimuth dependence of the FM rate and the third-order phase coefficient. It should be pointed out that before the azimuth processing, the small-aperture data need to be expanded by zero

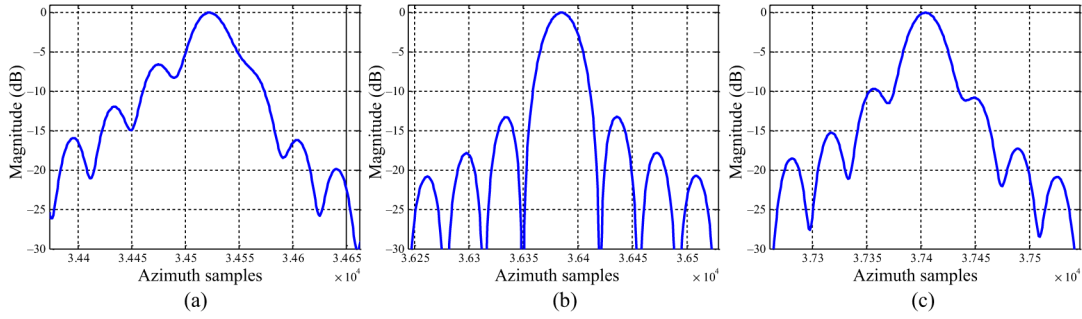


Fig. 7. Azimuth profiles of the three targets obtained by the reference algorithm. (a) Azimuth profile of target 1. (b) Azimuth profile of target 3. (c) Azimuth profile of target 5.

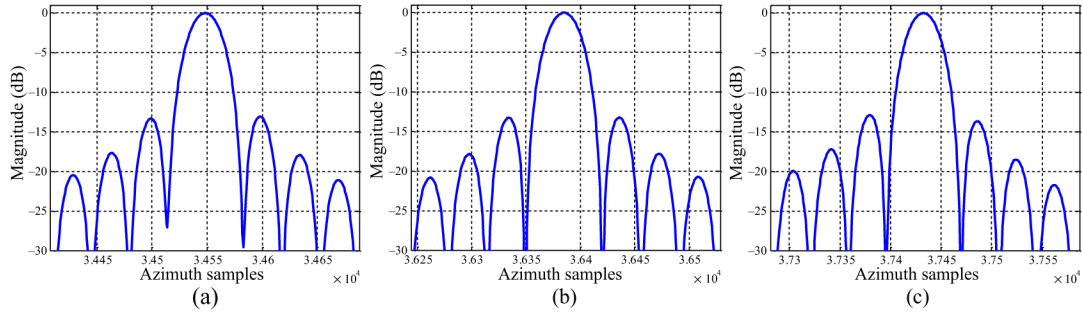


Fig. 8. Azimuth profiles of the three targets obtained by the proposed approach. (a) Azimuth profile of target 1. (b) Azimuth profile of target 3. (c) Azimuth profile of target 5.

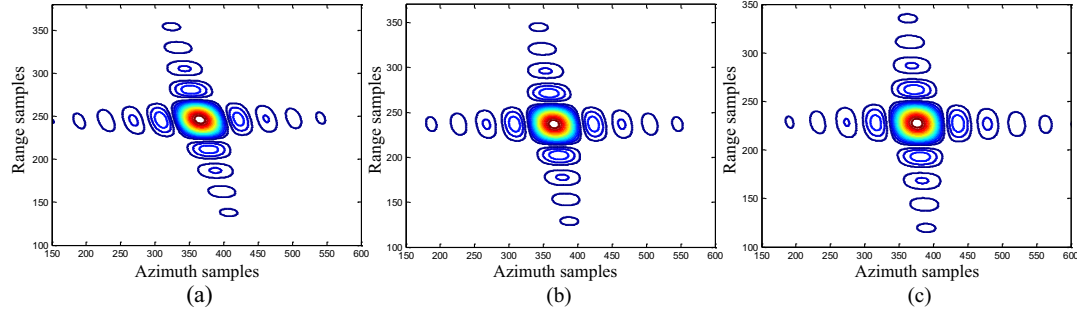


Fig. 9. Contour plots of the three targets. (a) Contour plot of target 1. (b) Contour plot of target 3. (c) Contour plot of target 5.

TABLE II
PERFORMANCE ANALYSIS OF THE SELECTED TARGETS

Parameters Point targets	Spatial resolution /m		PSLR/dB		ISLR/dB	
	Reference method	HPCA	Reference method	HPCA	Reference method	HPCA
p_1	3.1377	1.9368	-6.73	-13.22	-4.79	-9.67
p_3	1.9483	1.9481	-13.26	-13.26	-9.68	-9.68
p_5	2.6532	1.9485	-8.83	-13.24	-6.75	-9.60

padding operation in the time domain, since the small-aperture data support region is extended by the introduced correction phase. In the end, the SPECAN operation is done to implement the azimuth focusing. The simulated results and raw data processing validate the effectiveness of the presented approach.

However, it should be known that since the algorithm we proposed is used to focus only one small-aperture data, the full azimuth resolution cannot be reached. If we want to process a long azimuth strip, it is possible by mosaicking the subsequent detected small-aperture images.

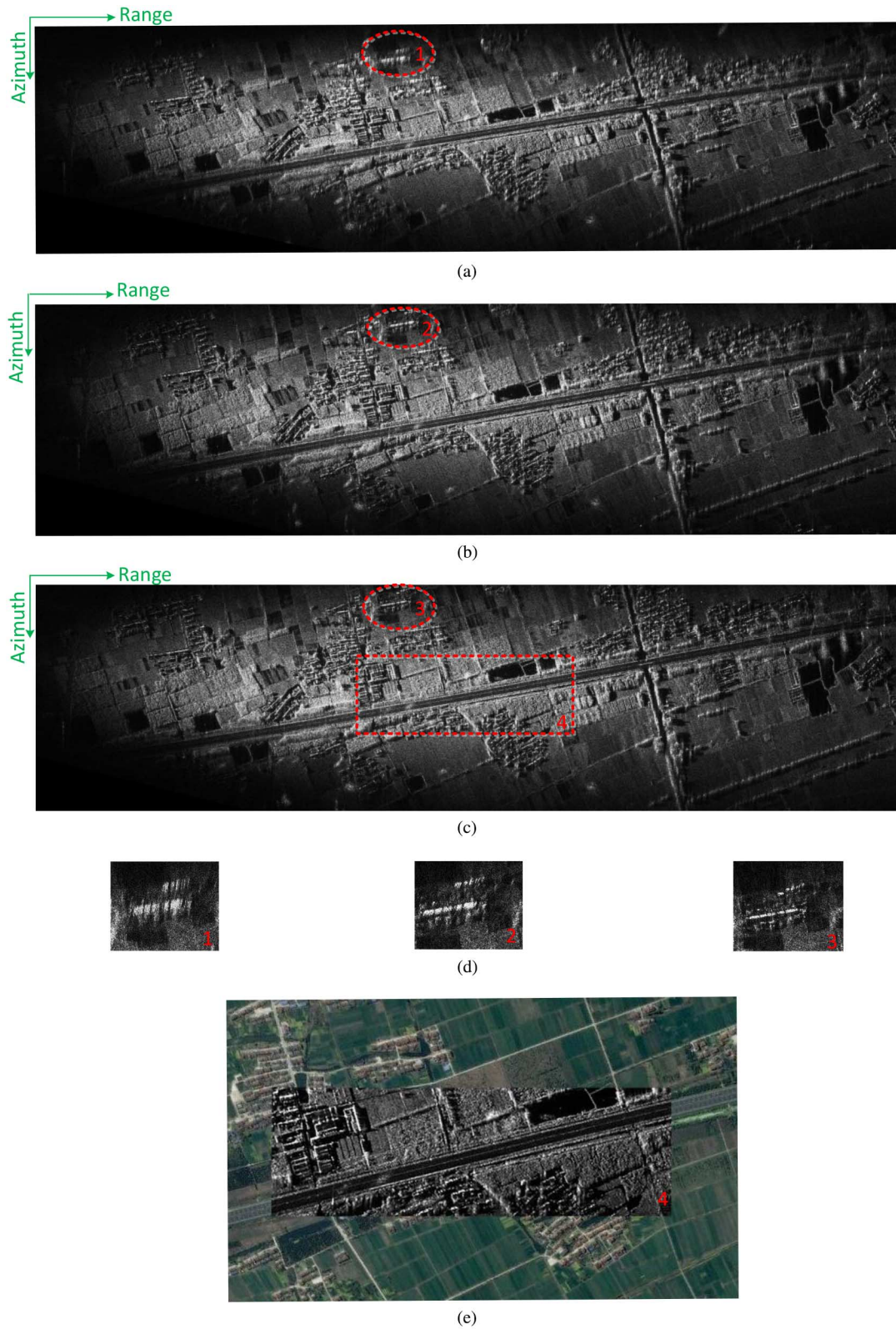


Fig. 10. Airborne HS-SAR raw data processing results by different azimuth focusing approaches. (a) Without the compensation for the azimuth dependence. (b) Result of the raw data processed by the reference algorithm. (c) Result of the raw data processed by the proposed approach. (d) Azimuth border of scene selected for comparison by the red-dashed oval from (a), (b), and (c). (e) Scene selected by the red-dashed rectangle from (c) is superpositioned on an optical image from the Google Earth Map.

APPENDIX A

After the LRWC, we transform the echo signal into the 2-D frequency domain, which yields

$$SS(f_r, f_a; R_0) = W_r(f_r) W_a(f_a) \exp\left(-j\pi \frac{f_r^2}{\gamma}\right) \cdot \exp\left(-j\frac{2\pi}{v} \left(f_a + f_{dc} + \frac{2v \sin \theta_0}{c} f_r\right) (R_0 \sin \theta_0 + x_n)\right) \cdot \exp\left(-j4\pi R_0 \cos \theta_0 \sqrt{\left(\frac{f_c + f_r}{c}\right)^2 - \left(\frac{f_a + f_{dc}}{2v} + \frac{\sin \theta_0}{c} f_r\right)^2}\right). \quad (A1)$$

In order to analyze the range curvature characteristic in depth, expand the square root terms of (A1) at $f_r = 0$ to its second-order Taylor series which has

$$\sqrt{\left(\frac{f_c + f_r}{c}\right)^2 - \left(\frac{f_a + f_{dc}}{2v} + \frac{\sin \theta_0}{c} f_r\right)^2} = \Phi_0 + \Phi_1 f_r + \Phi_2 f_r^2 \quad (A2)$$

$$\text{where } \Phi_0 = \sqrt{\left(\frac{f_c}{c}\right)^2 - \left(\frac{f_a + f_{dc}}{2v}\right)^2}, \quad \Phi_1 = \frac{\frac{f_c}{c^2} - \frac{(f_a + f_{dc}) \sin \theta_0}{2vc}}{\sqrt{\left(\frac{f_c}{c}\right)^2 - \left(\frac{f_a + f_{dc}}{2v}\right)^2}},$$

$$\text{and } \Phi_2 = -\frac{\left(\frac{f_c}{c} \sin \theta_0 - \frac{f_a + f_{dc}}{2v}\right)^2}{2c^2 \left(\left(\frac{f_c}{c}\right)^2 - \left(\frac{f_a + f_{dc}}{2v}\right)^2\right)^{\frac{3}{2}}}.$$

Substituting (A2) into (A1), the 2-D frequency-domain expression of the echo signal can be obtained, as shown in (4).

APPENDIX B

From (5), the azimuth signal phase is

$$\phi_{azi}(R'_0, x_n) = 4\pi R_0 \cos \theta_0 \Phi_0 + \frac{2\pi}{v} (f_a + f_{dc}) (R_0 \sin \theta_0 + x_n). \quad (B1)$$

Taylor series expansion of $\phi_{azi}(R'_0, x_n)$ at $f_a = 0$ yields

$$\phi'_0 = \phi_{azi}(R'_0, x_n)|_{f_a=0} = \frac{4\pi R'_0}{\lambda} \quad (B2)$$

$$\phi'_1 = \left. \frac{d\phi_{azi}(R'_0, x_n)}{df_a} \right|_{f_a=0} = \frac{2\pi x_n}{v} \quad (B3)$$

$$\phi'_2 = \left. \frac{d^2 \phi_{azi}(R'_0, x_n)}{df_a^2} \right|_{f_a=0} = -\frac{\pi \lambda (R'_0 - x_n \sin \theta_0)}{2v^2 \cos^2 \theta_0} \quad (B4)$$

$$\phi'_3 = \left. \frac{d^3 \phi_{azi}(R'_0, x_n)}{df_a^3} \right|_{f_a=0} = -\frac{\pi (R'_0 - x_n \sin \theta_0) \lambda^2 \sin \theta_0}{4v^3 \cos^4 \theta_0} \quad (B5)$$

$$\phi'_4 = \left. \frac{d^4 \phi_{azi}(R'_0, x_n)}{df_a^4} \right|_{f_a=0} = -\frac{\pi (R'_0 - x_n \sin \theta_0) \lambda^3 (1 + 4 \sin^2 \theta_0)}{32v^4 \cos^6 \theta_0}. \quad (B6)$$

ACKNOWLEDGMENT

The authors would like to thank the anonymous reviewers for their valuable suggestions to improve this paper.

REFERENCES

- [1] I. G. Cumming and F. H. Wong, *Digital Processing of Synthetic Aperture Radar Data*. Norwood, MA, USA: Artech House, 2005.
- [2] F. Zhang, A. Yu, F. He, and Z. Dong, "An improved DBS algorithm based on Doppler localization equations," in *Proc. IEEE China Summit Int. Conf. Signal Inf. Process.*, 2013, pp. 607–611.
- [3] F. Lili, W. Xuetian, and W. Yifeng, "A modified SPECAN algorithm for synthetic aperture radar imaging," in *Proc. Int. Conf. Measuring Technol. Mechatron. Autom.*, 2010, pp. 153–156.
- [4] T. Xiong, M. Xing, X. Xia, and Z. Bao, "New applications of omega-K algorithm for SAR data processing using effective wavelength at high squint," *IEEE Trans. Geosci. Remote Sens.*, vol. 51, no. 5, pp. 3156–3169, May 2013.
- [5] S.-Y. Tang, L.-R. Zhang, P. Guo, and Y.-H. Zhao, "An omega-K algorithm for highly squinted missile-borne SAR with constant acceleration," *IEEE Geosci. Remote Sens. Lett.*, vol. 9, no. 11, pp. 1569–1573, Jan. 2014.
- [6] S. Tang *et al.*, "Acceleration model analyses and imaging algorithm for highly squinted airborne spotlight-mode SAR with maneuvers," *IEEE J. Sel. Topics Appl. Earth Observ. Remote Sens.*, vol. 8, no. 3, pp. 1120–1131, Mar. 2015.
- [7] R. K. Raney, H. Runge, I. G. Cumming, R. Bamler, and F. H. Wong, "Precision of SAR processing using chirp scaling," *IEEE Trans. Geosci. Remote Sens.*, vol. 32, no. 4, pp. 786–799, Jul. 1994.
- [8] O. Frey *et al.*, "Focusing of airborne synthetic aperture radar data from highly nonlinear flight tracks," *IEEE Trans. Geosci. Remote Sens.*, vol. 47, no. 6, pp. 1844–1858, Jun. 2009.
- [9] F. H. Wong and T. S. Yeo, "New application of nonlinear chirp scaling in SAR data processing," *IEEE Trans. Geosci. Remote Sens.*, vol. 39, no. 5, pp. 946–953, May 2001.
- [10] X. L. Qiu, D. H. Hu, and C. B. Ding, "An improved NLCS algorithm with capability analysis for one-stationary BiSAR," *IEEE Trans. Geosci. Remote Sens.*, vol. 46, no. 10, pp. 3179–3186, Oct. 2008.
- [11] G.-C. Sun *et al.*, "A 2-D space-variant chirp scaling algorithm based on the RCM equalization and sub-band synthesis to process geosynchronous SAR data," *IEEE Trans. Geosci. Remote Sens.*, vol. 52, no. 8, pp. 4868–4880, Aug. 2014.
- [12] L. M. H. Ulander, H. Hellsten, and G. Stenstrom, "Synthetic-aperture radar processing using fast factorized back-projection," *IEEE Trans. Aerosp. Electron. Syst.*, vol. 39, no. 3, pp. 760–776, Mar. 2003.
- [13] G. Sun, M. Xing, Y. Liu, L. Sun, Z. Bao, and Y. Wu, "Extended NCS based on method of series reversion for imaging of highly squinted SAR," *IEEE Geosci. Remote Sens. Lett.*, vol. 8, no. 3, pp. 446–450, May 2011.
- [14] G.-C. Sun *et al.*, "Focus improvement of highly squinted data based on azimuth nonlinear scaling," *IEEE Trans. Geosci. Remote Sens.*, vol. 49, no. 6, pp. 2308–2322, Jun. 2011.
- [15] M. Xing, X. Jiang, R. Wu, F. Zhou, and Z. Bao, "Motion compensation for UAV SAR based on raw radar data," *IEEE Trans. Geosci. Remote Sens.*, vol. 47, no. 8, pp. 2870–2883, Aug. 2009.
- [16] W. Wang *et al.*, "Focus improvement of squint bistatic SAR data using azimuth nonlinear chirp scaling," *IEEE Geosci. Remote Sens. Lett.*, vol. 11, no. 1, pp. 229–234, Jan. 2014.
- [17] S.-X. Zhang *et al.*, "Focus improvement of high-squint SAR based on azimuth dependence of quadratic range cell migration correction," *IEEE Geosci. Remote Sens. Lett.*, vol. 10, no. 1, pp. 150–154, Jan. 2013.
- [18] D.-X. An *et al.*, "Extended nonlinear chirp scaling algorithm for high-resolution highly squint SAR data focusing," *IEEE Trans. Geosci. Remote Sens.*, vol. 50, no. 9, pp. 3595–3609, Sep. 2012.
- [19] D. Li *et al.*, "Extended azimuth nonlinear chirp scaling algorithm for bistatic SAR processing in high-resolution highly squinted mode," *IEEE Geosci. Remote Sens. Lett.*, vol. 11, no. 6, pp. 1134–1139, Jun. 2014.
- [20] G. Liu, P. Li, S. Tang, and L. Zhang, "Focusing highly squinted data with motion errors based on modified non-linear chirp scaling," *IET Radar Sonar Navig.*, vol. 7, no. 5, pp. 568–578, Jun. 2013.



Yi Liang was born in Shaanxi Province, China, in 1981. He received the B.S. and Ph.D. degrees in electrical engineering from Xidian University, Xi'an, China, in 2004 and 2009, respectively.

Currently, he is an Associate Professor with the National Laboratory of Radar Signal Processing, Xidian University. His research interests include synthetic aperture radar (SAR) imaging, GMTI, and real-time signal processing.



Mengdao Xing (M'04) was born in Zhejiang Province, China, in November 1975. He received the B.S. and Ph.D. degrees in electrical engineering from Xidian University, Xi'an, China, in 1997 and 2002, respectively.

Currently, he is a Full Professor with the National Laboratory of Radar Signal Processing, Xidian University. He is also with the National Key Laboratory of Microwave Imaging Technology, Institute of Electronics, Chinese Academy of Sciences, Beijing, China. He has authored or coauthored two books and published over 200 papers. His research interests include synthetic aperture radar (SAR), inversed SAR, and sparse signal processing.



Zhenyu Li was born in Lu'an, Anhui Province, China, in 1991. He received the B.S. degree in electronic engineering from Xidian University, Xi'an, China, in 2012. Currently, he is pursuing the Ph.D. degree in signal processing at the National Laboratory of Radar Signal Processing.

His research interests include SAR imaging and radar forward-looking imaging.



Zheng Bao (M'80–LSM'09) was born in Jiangsu, China. He received the Bachelor degree in radar engineering from Xidian University, Xi'an, China, in 1953.

Currently, he is a Professor with Xidian University, Xi'an, China, where he is also the Chairman of the Academic Board of the National Laboratory of Radar Signal Processing. He has authored or coauthored 6 books and published over 300 papers. His research fields include space-time adaptive processing, radar imaging (SAR/ISAR), automatic target recognition, and over-the-horizon-radar signal processing.



Letian Zeng was born in Xinxian, Henan Province, China, in 1988. He received the B.S. degree in electronic information engineering from the PLA Information Engineering University, Zhengzhou, China, in 2011. Currently, he is pursuing the Ph.D. degree in signal processing at the National Laboratory of Radar Signal Processing.

His research interests include airborne SAR imaging and motion compensation.